Novel D-shape LSPR fiber sensor based on nano-metal strips

Yue Jing He*

Department of Electronic Engineering, National Chin-Yi University of Technology, Taichung, Taiwan
*yuejing@ncut.edu.tw

Abstract: In this study, a novel D-shaped localized surface plasmon resonance (LSPR) fiber sensor was introduced. The construction of this sensor involved etching of a single-mode fiber on the cladding layer and core layer, followed by plating using nano-metal strips. The design and calculations of the entire sensor were based on a numerical simulation method combining the finite element method (FEM) and the eigenmode expansion method (EEM). By using graphical representations of the algorithm results, the excitation of the LSPR was clearly observed. The finished D-shaped LSPR fiber sensor possesses several excellent properties, including a short length (2494.4301 μm), high resolution (approximately 35 dB), and high sensitivity (approximately 20183.333 nm/RIU). In addition, compared with LPG-SPR fiber sensor, the framework provides three advantages, namely, a fabrication process that is compatible with semiconductor fabrication, as well as the low-temperature cross-talk and high-temperature stability of surface grating.

OCIS codes: (240.6680) Surface plasmons; (240.6690) Surface waves.

References and links

1. Y. J. He, "Investigation of LPG-SPR sensors using the finite element method and eigenmode expansion method," Opt. Express **21**(12), 13875–13895 (2013).
2. P. Bhatia and B. D. Gupta, "Surface-plasmon-resonance-based fiber-optic refractive index sensor: sensitivity enhancement," Appl. Opt. **50**(14), 2032–2036 (2011).
3. J. Cao, E. K. Galbraith, T. Sun, and K. T. V. Grattan, "Cross-Comparison of Surface Plasmon Resonance-Based Optical Fiber Sensors with Different Coating Structures," IEEE Sens. J. **12**(7), 2355–2361 (2012).
4. X. Yu, S. Zhang, Y. Zhang, H. P. Ho, P. Shum, H. Liu, and D. Liu, "An efficient approach for investigating surface plasmon resonance in asymmetric optical fibers based on birefringence analysis," Opt. Express **18**(17), 17950–17957 (2010).
5. M. Gu, P. Bai, and E. P. Li, "Enhancing the Reception of Propagating Surface Plasmons Using a Nanoantenna," IEEE Photon. Technol. Lett. **22**(4), 245–247 (2010).
6. L. Y. Shao, Y. Shevchenko, and J. Albert, "Intrinsic temperature sensitivity of tilted fiber Bragg grating based surface plasmon resonance sensors," Opt. Express **18**(11), 11464–11471 (2010).
7. K. H. An, M. Shtein, and K. P. Pipe, "Surface plasmon mediated energy transfer of electrically-pumped excitons," Opt. Express **18**(5), 4041–4048 (2010).
8. J. Wang, X. Chen, and W. Lu, "High-efficiency surface plasmon polariton source," J. Opt. Soc. Am. B **26**(12), B139–B142 (2009).
9. Y. S. Jung, J. Wuenschell, H. K. Kim, P. Kaur, and D. H. Waldeck, "Blue-shift of surface plasmon resonance in a metal nanoslit array structure," Opt. Express **17**(18), 16081–16091 (2009).
10. B. Spacková and J. Homola, "Theoretical analysis of a fiber optic surface plasmon resonance sensor utilizing a Bragg grating," Opt. Express **17**(25), 23254–23264 (2009).
11. D. Choi, I. M. Lee, J. Jung, J. Park, J. H. Han, and B. Lee, "Metallic-Grating-Based Interconnector Between Surface Plasmon Plariton Waveguides," J. Lightwave Technol. **27**(24), 5675–5680 (2009).
12. Y. C. Lu, W. P. Huang, and S. S. Jian, "Influence of Mode Loss on the Feasibility of Grating-Assisted Optical Fiber Surface Plasmon Resonance Refractive Index Sensor," J. Lightwave Technol. **27**(21), 4804–4808 (2009).
13. A. Wang, A. Docherty, B. T. Kuhlmey, F. M. Cox, and M. C. J. Large, "Side-hole fiber sensor based on surface plasmon resonance," Opt. Lett. **34**(24), 3890–3892 (2009).
14. Y. J. He, Y. L. Lo, and J. F. Huang, "Optical-fiber surface-plasmon-resonance sensor employing long-period fiber gratings in multiplexing," J. Opt. Soc. Am. B **23**(5), 801–811 (2006).
15. G. Nemova and R. Kashyap, "Modeling of Plasmon-Polariton Refractive-Index Hollow Core Fiber Sensors Assisted by a Fiber Bragg grating," J. Lightwave Technol. **24**(10), 3789–3796 (2006).

#190878 - $15.00 USD Received 21 May 2013; revised 10 Aug 2013; accepted 13 Sep 2013; published 26 Sep 2013

16. Ó. Esteban, R. Alonso, M. C. Navarrete, and A. González-Cano, "Surface Plasmon Excitation in Fiber-Optics Sensors: A Novel Theoretical Approach," J. Lightwave Technol. **20**(3), 448–453 (2002).
17. H. Y. Lin, C. H. Huang, G. L. Cheng, N. K. Chen, and H. C. Chui, "Tapered optical fiber sensor based on localized surface plasmon resonance," Opt. Express **20**(19), 21693–21701 (2012).
18. R. Dutta, R. Bharadwaj, S. Mukherji, and T. Kundu, "Study of localized surface-plasmon-resonance-based optical fiber sensor," Appl. Opt. **50**(25), E138–E144 (2011).
19. Y. Lin, Y. Zou, and R. G. Lindquist, "A reflection-based localized surface plasmon resonance fiber-optic probe for biochemical sensing," Biomed. Opt. Express **2**(3), 478–484 (2011).
20. C. Y. Tsai, S. P. Lu, J. W. Lin, and P. T. Lee, "High sensitivity plasmonic index sensor using slablike gold nanoring arrays," Appl. Phys. Lett. **98**(15), 153108 (2011).
21. S. K. Srivastava and B. D. Gupta, "Simulation of a localized surface-plasmon-resonance-based fiber optic temperature sensor," J. Opt. Soc. Am. A **27**(7), 1743–1749 (2010).
22. R. Marty, G. Baffou, A. Arbouet, C. Girard, and R. Quidant, "Charge distribution induced inside complex plasmonic nanoparticles," Opt. Express **18**(3), 3035–3044 (2010).
23. M. J. Kofke, D. H. Waldeck, and G. C. Walker, "Composite nanoparticle nanoslit arrays: a novel platform for LSPR mediated subwavelength optical transmission," Opt. Express **18**(8), 7705–7713 (2010).
24. W. Y. Ma, H. Yang, J. P. Hilton, Q. Lin, J. Y. Liu, L. X. Huang, and J. Yao, "A numerical investigation of the effect of vertex geometry on localized surface plasmon resonance of nanostructure," Opt. Express **18**(2), 843–853 (2010).
25. V. V. R. Sai, T. Kundu, and S. Mukherji, "Novel U-bent fiber optic probe for localized surface plasmon resonance based biosensor," Biosens. Bioelectron. **24**(9), 2804–2809 (2009).
26. H. Y. Lin, C. H. Huang, C. H. Chang, Y. C. Lan, and H. C. Chui, "Direct near-field optical imaging of plasmonic resonances in metal nanoparticle pairs," Opt. Express **18**(1), 165–172 (2010).
27. S. J. Yoon and D. Kim, "Target dependence of the sensitivity in periodic nanowire-based localized surface plasmon resonance biosensors," J. Opt. Soc. Am. A **25**(3), 725–735 (2008).
28. S. K. Srivastava, R. K. Verma, and B. D. Gupta, "Theoretical modeling of a localized surface plasmon resonance based intensity modulated fiber optic refractive index sensor," Appl. Opt. **48**(19), 3796–3802 (2009).
29. D. F. G. Gallagher and T. P. Felici, "Emgenmode expansion methods for simulation of optical propagation in photonics-Pros and cons," Proc. SPIE **4987**, 69–82 (2003).
30. M. Y. Ng and W. C. Liu, "Fluorescence enhancements of fiber-optic biosensor with metallic nanoparticles," Opt. Express **17**(7), 5867–5878 (2009).
31. E. D. Palik, *Handbook of Optical* Constants *of Solids* (Academic Press, 1985).
32. J. Renger, "Excitation, interaction, and scattering of localized and propagating surface polaritons," Ph.D. Thesis., Technical University, Dresden, (2006).
33. M. Hu, J. Y. Chen, Z. Y. Li, L. Au, G. V. Hartland, X. D. Li, M. Marquez, and Y. N. Xia, "Gold nanostructures: engineering their plasmonic properties for biomedical applications," Chem. Soc. Rev. **35**(11), 1084–1094 (2006).

1. Introduction

Over the past several years, numerous optical-fiber surface plasmon sensors have been introduced to reduce the size of sensors. Optical-fiber surface plasmon sensors can be grouped into two main categories, depending on their plasmon resonances phenomenon. Surface plasmon resonance (SPR) is a resonance phenomenon that involves the surface charge density wave of free electrons in a metal [1–16]. It provides highly sensitive and label-free biosensing for probing the affinity between biological molecules, and has been widely used in biology, biochemistry, and genetic engineering in the last decade. Localized surface plasmon resonance (LSPR) is another resonance phenomenon involving free electron waves in a metal [17–31], occurring in metallic nanostructures such as nanoparticles and nanometer-scale rough surfaces. In this study, a D-shaped LSPR fiber sensor based on nano-metal strips was introduced. The side and cross-sectional structure diagrams of the sensor are shown in Fig. 1 and Fig. 2, in which Segment (a) is a general single-mode fiber (SMF), whereas Segment (b) is a D-shaped structure that was formed by first etching the upper portion of the cladding layer in Segment (a) and then plating with a metal material of a d_m thickness. For Segment (c), following the etching of the upper portion of the cladding layer, the subsequent core layer was etched for a thickness of d_m and then plated with a metal material of d_m thickness. The structural parameters of the D-shaped LSPR fiber sensor were: $a_1 = 2.25$ μm, $a_2 = 5.25$ μm, $d_1 = 2.23$ μm, $d_m = 0.02$ μm, $n_1 = 1.454$, $n_2 = 1.43$, $n_m = 0.56246309 + j9.840798407$ ($\lambda = 1550$ nm), $n_a = 1.33$, $\Lambda = 1.508321$ μm, $N = 1614$, $L_1 = 30$ μm, $L_2 = N*\Lambda = 2434.4301$ μm, $L_3 = 30$ μm. The thickness of the analyte is $d_a = 1$ μm. The total length of the entire D-shaped LSPR fiber sensor was $L = L_1 + L_2 + L_3 = 2494.4301$ μm. The total length of x axis (and that of y axis) used to simulated is 12.5 μm. Gold was used as the material for the metallic layer in this study. The complex refractive index of gold was obtained from the Handbook of Optical

#190878 - $15.00 USD Received 21 May 2013; revised 10 Aug 2013; accepted 13 Sep 2013; published 26 Sep 2013

Constants of Solids (Academic Orlando FL, 1998) [14], and its precise wavelength-dependent fit to the data within was determined using a cubic spline algorithm. The plot of the complex refractive index for gold can be found in Fig. 1 [1].

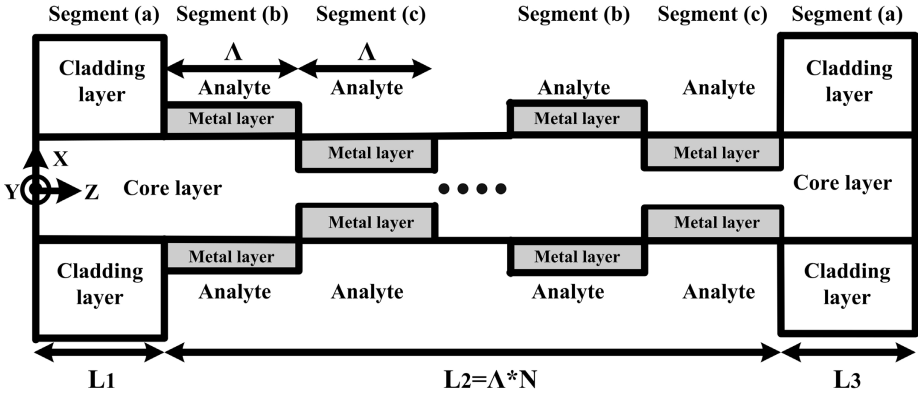

Fig. 1. D-shaped LSPR fiber sensor side view structural diagram.

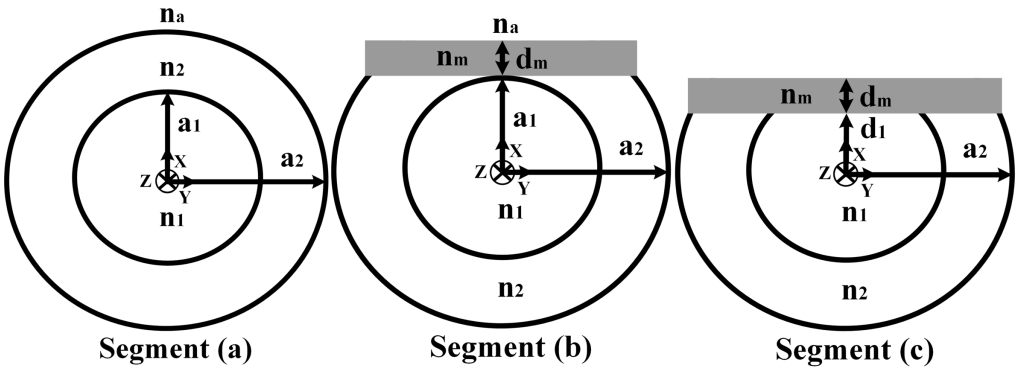

Fig. 2. D-shaped LSPR fiber sensor sectional view structural diagram.

D-shaped LSPR fiber sensor is a very sensitive component for self-structure parameters, operating wavelength, and the variation of the refractive index of the analyte. Therefore, in the scope of D-shaped LSPR fiber sensor, it is well-known that we have to understand beforehand the responses of D-shaped LSPR fiber sensor for the above parameters before starting to construct LSPR fiber sensor actually. This study employed a numerical technique that combines finite element method (FEM) and eigenmode expansion method (EEM) in the D-shaped LSPR fiber sensor design and simulation, and shows that by using this numerical technique, the design and analysis of D-shaped LSPR fiber sensor can be effortlessly accomplished without using any mathematical equations by novice learners and application-level designers. In addition, the extensive use of graphics may help novice learners and application-level designers visually understand the transmission of optical signals in D-shaped LSPR fiber sensor. Furthermore, the method introduced in the present study may be widely applied to component designs that have a periodic structure.

The remainder of this paper is divided into the following sections: Section II provides a brief introduction to theories related to the FEM. From the perspective of numerical methods, the decomposition resolution of triangular elements inevitably influences the correctness of the acquired modes. From a mathematical perspective, if all obtained modes are accurate, the orthogonal values between the modes must be 0. Thus, we used the reverse-thinking method to determine the allowable orthogonal value, which was 10^{-4} ($\log_{10}(10^{-4}) = -4$dB), before adjusting the decomposition resolutions to perform simulations.

#190878 - $15.00 USD Received 21 May 2013; revised 10 Aug 2013; accepted 13 Sep 2013; published 26 Sep 2013

Section III introduces the theories related to the EEM. A detailed description is provided to explain how the EEM enables guided modes to conduct transmission in D-shaped LSPR fiber sensor. However, this numerical method also has problems regarding accuracy. The Fourier series expansion is the main principle that enabled light wave transmissions to be performed using this numerical method. That is, if the number of modes was insufficient during the transfer process, even in non-absorbent media, the total power would decline as the number of implementing Fourier series expansion increased. We used the reverse thinking method to employ different numbers of guided modes to perform transmissions, consider the power lost, and determine the number of guided modes for this study. Here, we must emphasize that for non-absorbent media, the power lost in transmission distances is typically used to determine the sufficient mode quantity. However, that light wave power attenuates with distance in absorbent materials is a natural phenomenon. To determine the power loss caused by the Fourier series expansion, we should consider the original definition of loss. That is, observe the power loss conditions for every position of the Fourier series expansion execution. Because of the presence of gold and the absorbent material used in the structure for this study, when designing and analyzing the D-shaped LSPR fiber sensor, we checked the power losses of all Fourier series expansion positions according to the basic definition of loss to verify the legitimacy of the eigenmode expansion method.

In Section IV, we summarize the content of Sections II and III to propose a rigorous, simple, and complete design process for analyzing and designing D-shaped LSPR fiber sensor. Additionally, we employ numerous graphics to present the simulation results.

In the final section, we summarize the numerical simulation method used in this study, and use the data obtained in Section IV to verify that the proposed novel D-shaped LSPR fiber sensor possesses excellent attributes of short length (2494.4301 μm), high resolution (approximately 35 dB), and high sensitivity (approximately 20183.333 nm/RIU).

2. Finite element method

The FEM is a numerical method used to solve partial differential equations (PDE) that satisfy boundary conditions. This method is based on the variational principle, domain decomposition, and interpolation function. The FEM uses the variation principle (the variation algorithm) to transform the original problem (PDE with boundary conditions) into functional extreme value problems different from the original problem but with equivalent values. In other words, the same physical problem has two mathematical descriptions. That is, "boundary conditions + PDE= the functional for determining the minimum value." After determining the functional extreme value problem equivalent to the original problem, we applied the interpolation function and decomposed the domain we hoped to solve to convert the problem in which the functional solved for the minimum value into a set of multiple linear algebraic equations. We can obtain the solution to the original problem by solving these linear algebraic equations.

In this study, we use the triangular element method to decompose the geometric domain of the X-Y plane of optical fibers, as shown in Fig. 2. A higher decomposition resolution results in more accurate results, although the process involves significantly more computations. Therefore, appropriate discretization of the target solution domain is a vital technique when applying the FEM. As mentioned previously regarding the relationship between the obtained modes and decomposition resolution, theoretically, all modes must be mutually orthogonal. The orthogonal values can be represented using the following equation [1]:

$$\int_{A\infty} \vec{E}_{t\nu} \times \vec{H}_{t\mu} \bullet \hat{z}\, dA = \int_{A\infty} \vec{E}_{t\mu} \times \vec{H}_{t\nu} \bullet \hat{z}\, dA = 0 \quad for \quad \nu \neq \mu. \tag{1}$$

However, regarding numerical simulations, problems such as an extremely large memory capacity and long mode solution time are inevitable. To accommodate the server's computational capacity, we reviewed the orthogonal values of the obtained modes to adjust the resolution of triangular decomposition appropriately. Unless otherwise indicated, all the decomposition resolutions in this study have orthogonal values that are smaller than 10^{-4}

#190878 - $15.00 USD Received 21 May 2013; revised 10 Aug 2013; accepted 13 Sep 2013; published 26 Sep 2013

($\log_{10}(10^{-4})$ = –4dB). Following decomposition, we can solve all guided modes in three segments, with an operating wavelength ofλ = 1550 nm. Because single-mode optical fibers were used, we obtained only one core mode, that is, HE_{11}, with an effective refractive index of n_{eff}^{core} ($n_2 < n_{eff}^{core} < n_1$), and many numbers of cladding modes, with an effective refractive index of $n_{eff}^{cladding}$ ($n_a < n_{eff}^{cladding} < n_2$).

We initially obtained 50 guided modes comprising one core mode HE_{11} and 49 cladding modes, $\nu = 1-49$. According to the structural diagram of metal (Au) in D-shaped LSPR fiber sensor (as shown in Fig. 3), in this manuscript the 2D power distribution of the first LSPR wave solved by FEM for the thickness of 20 nm (Au) on the x axis was shown in Fig. 4. Obviously, an analogous dipole is excited in this novel LSPR fiber sensor and it clearly explains that the current metallic patterns in the fiber sensor can trigger the LSPR by the electric field E_X of the core mode HE_{11}. For the length (9.5μm) on the y axis and that (Λ = 1.508321μm) on the z axis, the LSPRs triggered by the electric field E_Y and E_Z of the core mode HE_{11}, respectively, are rather weaker than on the x axis. In other words, in this novel LSPR fiber sensor the physical phenomenon of LSPR excited for the waveguides, segment (b) and segment (c), is on the x axis and it dominates the LSPR of the waveguides [32,33].

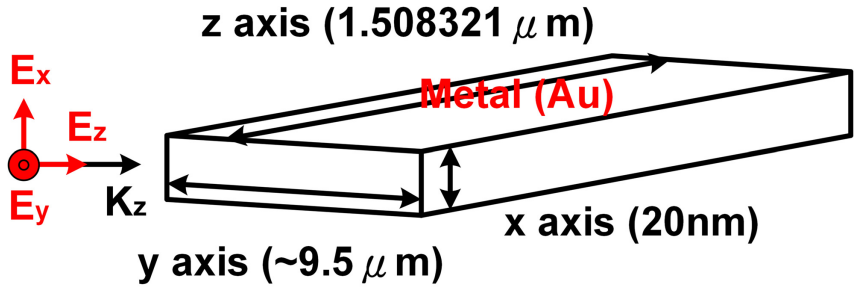

Fig. 3. The structural diagram of metal (Au) in D-shaped LSPR fiber sensor.

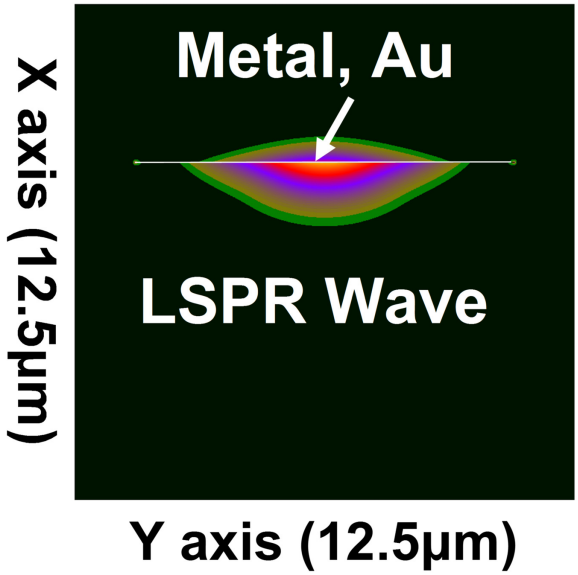

Fig. 4. The 2D power distribution of the first LSPR wave for the thickness of 20 nm (Au) on the x axis.

#190878 - $15.00 USD Received 21 May 2013; revised 10 Aug 2013; accepted 13 Sep 2013; published 26 Sep 2013

3. Eigenmode expansion method

The primary objective of this method was to induce the guided mode to transmit power in the fiber structure. Each segment object is considered a uniform waveguide possessing a fixed refractive index value. The contact surface between segment object k-1 (Se_{k-1}) and segment object k (Se_k) is called junction k-1 (J_{k-1}). The power conversions between segment objects were performed using the Fourier series expansion method. The steps in this procedure can also be performed to complete the power transfers of the entire D-shaped LSPR fiber sensor.

This process indicates that the guided modes existing in the same segment of a periodic component are identical. Therefore, when the FEM is used to solve guided modes, it suffices to calculate only one segment. This significantly reduces the computation time and memory consumed during the entire component simulation. In conclusion, the combination of the FEM and the EEM is particularly suitable for designing periodic components.

Below we explain how the EEM is applied to D-shaped LSPR fiber sensor power propagation. We hypothesized that the solution of the Maxwell equations in each uniform waveguide (segment) is equivalent to Eq. (2), where the mode content Φ_n and propagation constant β_n are eigenfunctions and eigenvalues obtained from the FEM.

$$E(x,y,z) = \Phi_n(x,y)e^{i\beta_n z} \tag{2}$$

By combining Eq. (2) with the Fourier series expansion concept, and adding the entire forward propagation mode $Se_k^{(+)}$, as shown in Eq. (3), and the back propagation mode $Se_k^{(-)}$, as shown in Eq. (4), where $m = 50$ was the guided mode amount, and C_n^f and C_n^b were the coefficients for each forward and backward mode field, as shown in Fig. 5, the electric and magnetic fields within the uniform segment object Se_{k-1} can be obtained, as shown in Eq. (5) and Eq. (6).

$$Se_k^{(+)} = \sum_{n=1}^{m} C_n^f \Phi_n(x,y)e^{i\beta_n z} \tag{3}$$

$$Se_k^{(-)} = \sum_{n=1}^{m} C_n^b \Phi_n(x,y)e^{-i\beta_n z} \tag{4}$$

$$E(x,y,z) = \sum_{n=1}^{m} (C_n^f e^{i\beta_n z} + C_n^b e^{-i\beta_n z})E_n(x,y) \tag{5}$$

$$H(x,y,z) = \sum_{n=1}^{m} (C_n^f e^{i\beta_n z} + C_n^b e^{-i\beta_n z})H_n(x,y) \tag{6}$$

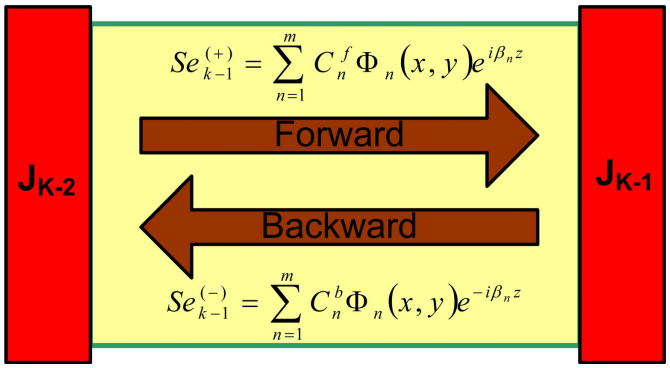

Fig. 5. Fourier series expansion for the forward and backward propagation modes.

#190878 - $15.00 USD Received 21 May 2013; revised 10 Aug 2013; accepted 13 Sep 2013; published 26 Sep 2013

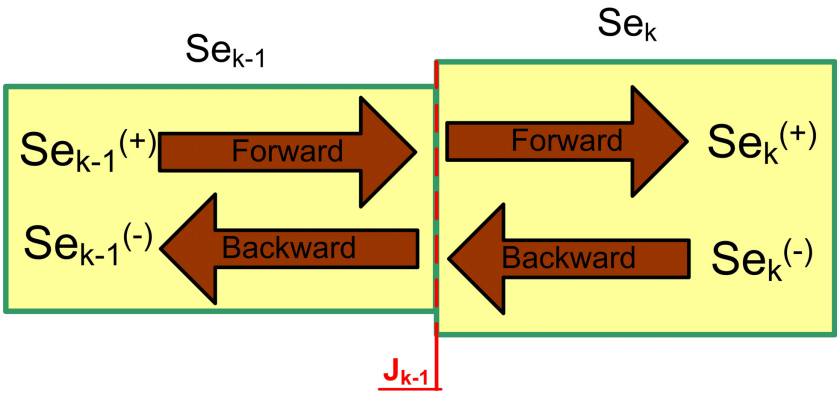

Fig. 6. The relationship between the field strength of the two adjacent uniform segment objects Se_{k-1} and Se_k.

After the propagated electromagnetic fields for a uniform segment object Se_{k-1} are obtained, power must be precisely transferred from segment object Se_{k-1} to segment object Se_k. Here, we used the scattering matrix to transform the forward and backward power propagation of two adjacent segment objects, as shown in Eq. (7). In Fig. 6, $Se_{k-1}^{(+)}$, $Se_k^{(+)}$ and $Se_{k-1}^{(-)}$, $Se_k^{(-)}$ were the total of the forward and backward propagation modes for the uniform segment object Se_{k-1} and the uniform segment object Se_k, and J_{k-1} was the scattering matrix of the adjacent segment object junctions.

$$\begin{bmatrix} Se_{k-1}^{(-)} \\ Se_k^{(+)} \end{bmatrix} = J_{k-1} \begin{bmatrix} Se_{k-1}^{(+)} \\ Se_k^{(-)} \end{bmatrix} \tag{7}$$

To convert power between adjacent segment objects, we employed the Fourier series expansion to obtain the unknown junction scattering matrix J_{k-1}. Finally, the propagation effects of D-shaped LSPR fiber sensor could be accurately conducted and completed by following the steps of this method. According to the detailed description of the EEM, we determined that in Eqs. (3) to (6), m represents the number of guided modes and can critically affect the accuracy of the method. From a mathematical perspective, the Fourier series expansion must include all the guided modes that existed in the structure. However, this is impossible for numerical simulations because the time and memory required to perform such calculations are excessive and cannot be tolerated. However, if the number of modes is insufficient, some power loss will occur during each pass through the scattering matrix for the adjacent segment object junction. Therefore, for this study, we employed the reverse thinking method, and searched for the minimum m value that satisfied the requirement that the power loss value could not exceed 10^{-4} ($\log_{10}(10^{-4}) = -4$dB).

4. Design and simulation of D-shape LSPR Fiber Sensor

Summarizing the numerical simulation methods described in Sections II and III, in this section we proposed a rigorous and simplistic design process to complete the analysis and design of D-shaped LSPR fiber sensor. This mechanism essentially comprises the following six procedures: (a) solve for the guided modes using the FEM; (b)verify whether the guided modes obtained using FEM satisfies the less than 10^{-4} ($\log_{10}(10^{-4}) = -4$dB) specification for orthogonal values; (c) use the EEM to perform an algorithm for power transmission; (d) test whether the power loss obtained using the EEM satisfies the less than 10^{-4} ($\log_{10}(10^{-4}) = -4$dB) specification; (e) calculate the resolution of the D-shaped LSPR fiber sensor; and (f) calculate the sensitivity of the sensor. All numerical calculations in this study were conducted using 50 modes.

#190878 - $15.00 USD Received 21 May 2013; revised 10 Aug 2013; accepted 13 Sep 2013; published 26 Sep 2013

The three uniform waveguides (Segments (a) to (c) in Fig. 1) were separately calculated to test the orthogonality of the guided modes obtained using FEM in this structure. The orthogonal values among the 50 modes were calculated and examined; the results are shown in Fig. 7. Clearly, besides each mode having a self-orthogonal value of 1, the orthogonal values between two modes could satisfy the requirement of being less than 10^{-4} ($\log_{10}(10^{-4})$ = −4dB). After the D-shaped LSPR fiber sensor was designed based on the above parameters, the core mode (as shown in Fig. 8) was inputted in the left end of Fig. 1. The power transmission (Poynting vector P_Z) algorithm was then conducted using EEM, and the results are shown in Fig. 9(a). To further observe the newly structured LSPR, the View A region in Fig. 9(a) was magnified, as shown in Fig. 9(b), which clearly indicates the excitation of the LSPR.

In addition, the 2D and 3D power distribution graphs were plotted for a location of Z = 63.569 μm, as shown in Fig. 10. Certainly, the loss of all mode expansion positions must satisfy the requirement of less than 10^{-4} ($\log_{10}(10^{-4})$ = −4dB) for employing the 50 guided modes. Figure 11 shows the calculation results of the mode expansion positions and power loss, which evidently satisfy the requirement of the aforementioned specification. Resolution and sensitivity are two important indicators for evaluating the quality of any sensor. In this study, these indicators are presented in detail using the calculation results of the D-shaped LSPR fiber sensor spectrum.

#190878 - $15.00 USD Received 21 May 2013; revised 10 Aug 2013; accepted 13 Sep 2013; published 26 Sep 2013

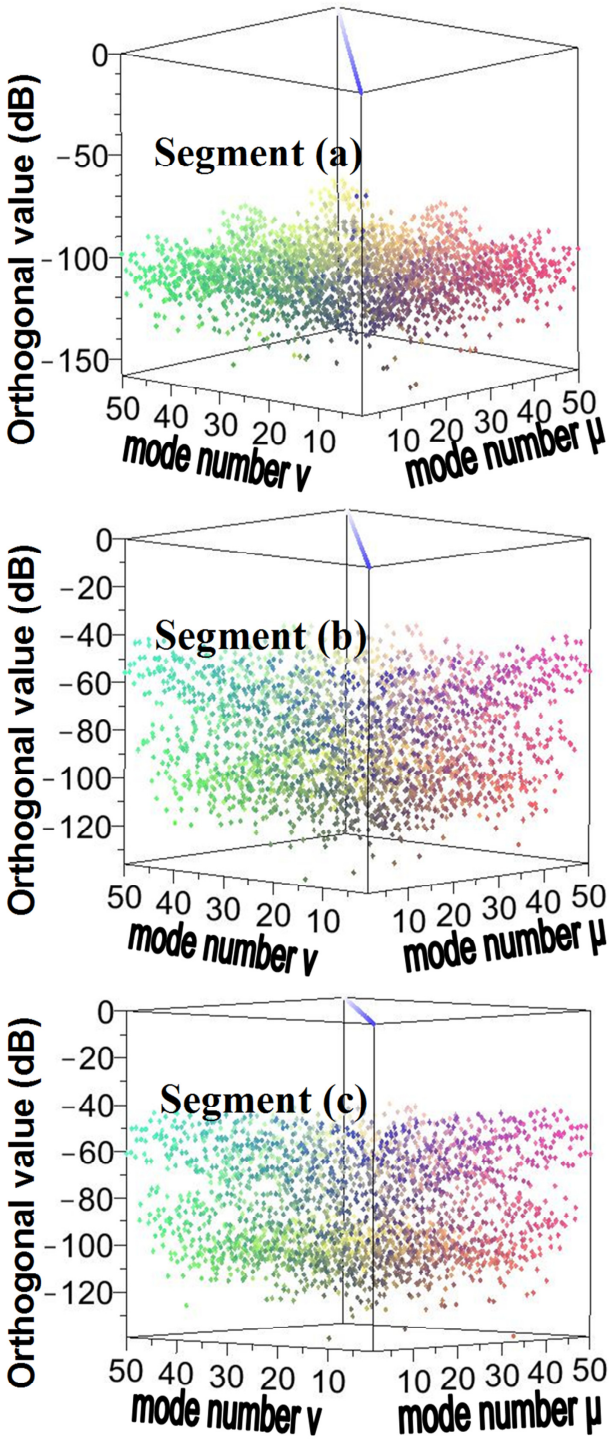

Fig. 7. The relationships between the orthogonal values of the 50 modes in segment (a), segment (b), and segment (c).

#190878 - $15.00 USD Received 21 May 2013; revised 10 Aug 2013; accepted 13 Sep 2013; published 26 Sep 2013

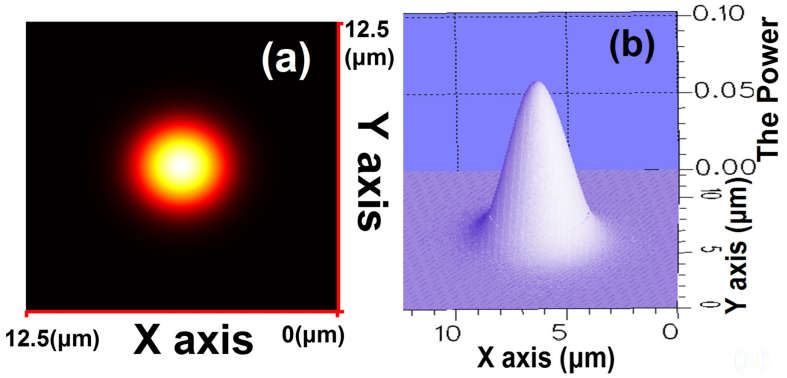

Fig. 8. The 2D and 3D power distribution of the core mode; the effective refractive index is $n_{eff}^{core} = 1.442631$. The total length of x axis (and that of y axis) used to simulated is 12.5 μm.

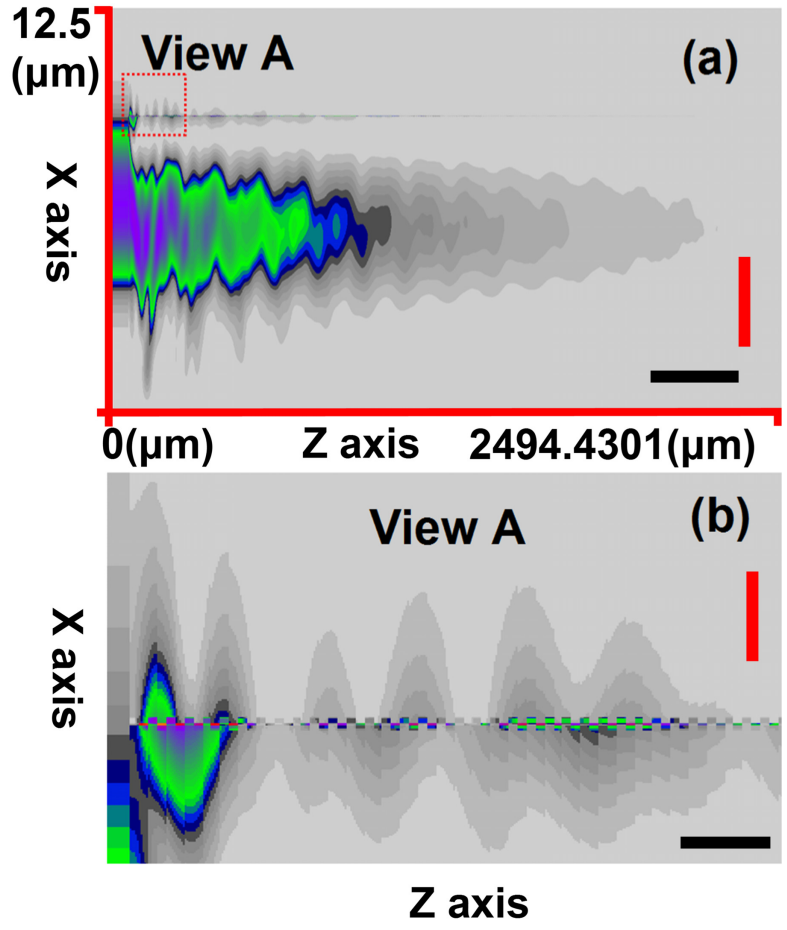

Fig. 9. (a) The X-Z plane power transmission (Poynting Vector P_Z) of the core mode, and (b) A magnified image of the View A region in (a) with scale bar 7 and 60 μm for z axis and scale bar 7 and 35 μm for x axis.

#190878 - $15.00 USD Received 21 May 2013; revised 10 Aug 2013; accepted 13 Sep 2013; published 26 Sep 2013

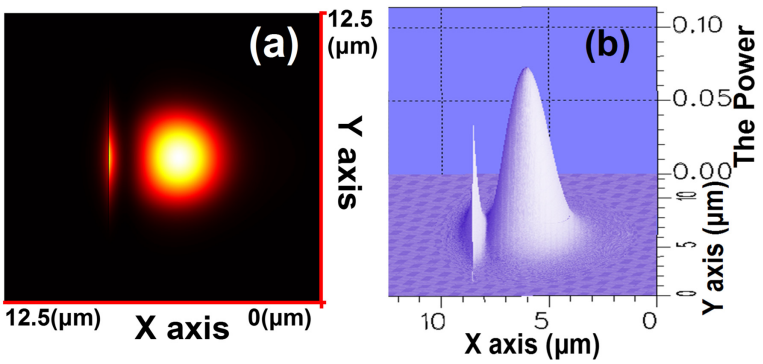

Fig. 10. The 2D and 3D power distribution of the D-shape LSPR sensor at z = 63.569 μm. The total length of x axis (and that of y axis) used to simulated is 12.5 μm.

As far as the actual spectrum measurement of the D-shaped LSPR fiber sensor is concerned, the instrument, OSA, is used most frequently. How can we recognize which one is the resonance dip of the D-shaped LSPR fiber sensor against the noise? Obviously, the meaning of the resolution used in D-shaped LSPR fiber sensor is the ability of recognizing the resonance dip of the D-shaped LSPR fiber sensor against the noise for OSA. In addition, it is well-known that in the spectrum diagram the shift ability of resonance wavelength denotes the sensitivity of D-shaped LSPR fiber sensor when the refractive index of an analyte changes.

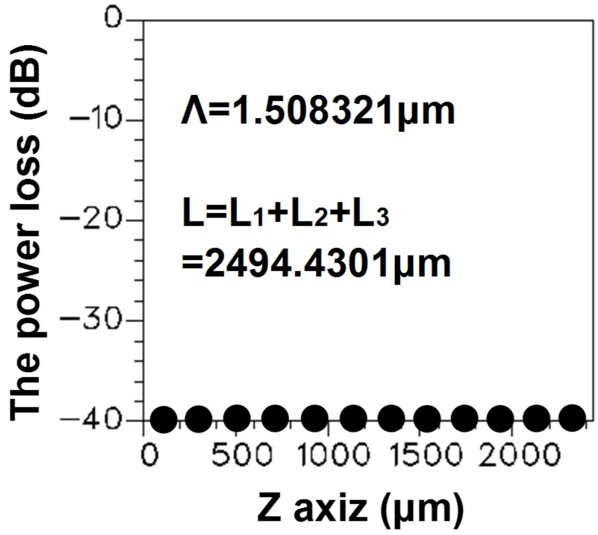

Fig. 11. The relationships between the eigenmode mode expansion position and power loss for employing the 50 guided modes.

To analyze the spectral characteristic of the D-shaped LSPR fiber sensor, the bar transmission power is used as the following mathematical equation [1]:

$$t_{=} = \frac{|R(z)|^2}{|R(0)|^2}. \tag{8}$$

Simply put, the bar transmission power is the self-power ratio of the incident core mode after traveling a certain distance (z) and when incidence occurs (z = 0). Calculations for the core mode spectral patterns of various analytes using Eq. (8) are shown in Fig. 12. Specifically, the analyte refractive index changed from n_a = 1.327 to n_a = 1.333. An observation of Fig. 12 shows that this novel D-shaped LSPR fiber sensor possesses a high

#190878 - $15.00 USD Received 21 May 2013; revised 10 Aug 2013; accepted 13 Sep 2013; published 26 Sep 2013

resolution of approximately 35 dB. Figure 13 indicates a diagram illustrating the relationship between resonance wavelength and the analyte refractive index in Fig. 12. From Fig. 13, the resonance wavelength of D-shaped LSPR fiber sensor shifted from 1.4953μm to 1.6164μm when the analyte refractive index changed from n_a = 1.327 to n_a = 1.333. Consequently, the sensitivity can be calculated as shown the following:

$$\text{Sensitivity} \approx \frac{(1.6164-1.4953)}{(1.333-1.327)} \approx 20183.333(\frac{\text{nm}}{\text{RIU}}) \tag{9}$$

where RIU is refractive index unit. This figure demonstrates that the novel D-shaped LSPR fiber sensor possesses a significantly high sensitivity of approximately 20183.333 nm/RIU.

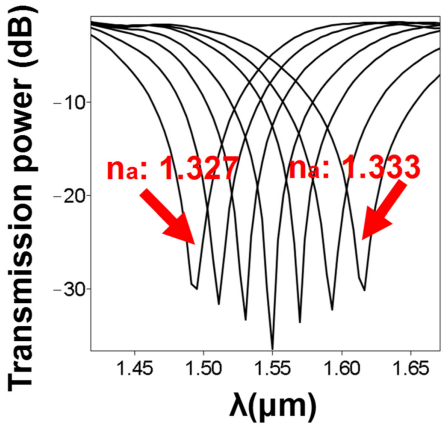

Fig. 12. Spectrum changes for the D-shaped LSPR fiber sensor when the analyte refractive index n_a changed.

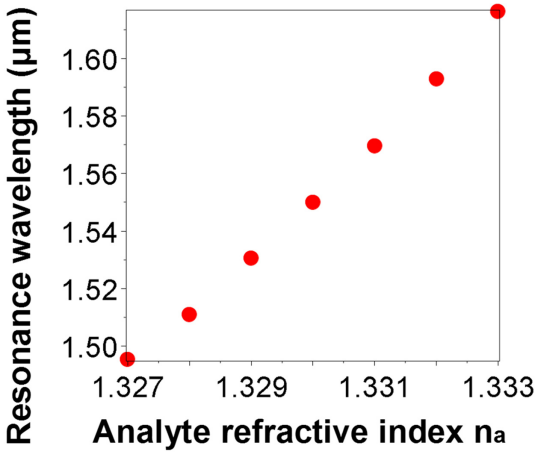

Fig. 13. The relationships between the analyte refractive index n_a and the D-shaped LSPR's resonance wavelength.

5. Conclusion

A novel D-shaped LSPR fiber sensor based on nano-metal strips was introduced. By combining the FEM and EEM numerical simulation methods, the design and analysis of the D-shaped LSPR fiber sensor were easily accomplished. Using the simulated results, the LSPR phenomenon could clearly be observed, and a D-shaped LSPR fiber sensor featuring a short

#190878 - $15.00 USD Received 21 May 2013; revised 10 Aug 2013; accepted 13 Sep 2013; published 26 Sep 2013

length (2494.4301 μm), high resolution (approximately 35 dB), and high sensitivity (approximately 20183.333 nm/RIU) could be completed. In addition, compared with LPG-SPR fiber sensor, the framework provides three advantages, namely, a fabrication process that is compatible with semiconductor fabrication, as well as the low-temperature cross-talk and high-temperature stability of surface grating. In consideration of extant SPR sensors that are highly sensitive and obtain smaller size, future studies will be focused on optimizing the structure of this D-shaped LSPR fiber sensor, such as etching thickness, the length ratio between Segment (b) and Segment (c) (i.e., the duty cycle), and the thickness and material of the metal plating to improve the sensitivity of this sensor. Furthermore, the temperature response is a crucial aspect for the sensor. Thus, this topic requires further investigation. The author endeavors to construct a model for investigating the effects that the geometric structure parameters and optical parameters have on temperature, and integrate this model with the FEM and EEM to determine the temperature response of the proposed D-shaped LSPR fiber sensor.

Acknowledgment

The author gratefully acknowledges the support provided to this study by the National Science Council (NSC101-2622-E-007-CC3) of Taiwan. In addition, the author gratefully acknowledges the rather worthwhile comments provided by Professor, Wei-Ching Chuang.

#190878 - $15.00 USD Received 21 May 2013; revised 10 Aug 2013; accepted 13 Sep 2013; published 26 Sep 2013